

# Chapter 10

## Magnetic Field Forward Models

*Biot-Savart Physics, Conditioning Analysis, and the Depth-Amplitude Ambiguity*

This chapter develops the **magnetic forward model operator**  $\mathcal{G}_B$ , which maps current density distributions  $\mathbf{J}(\mathbf{r})$  to magnetic field measurements  $\mathbf{B}(\mathbf{r})$  via the Biot-Savart law. The fundamental task is **physics-based source-to-field mapping**: establishing the mathematical relationship that enables current reconstruction from magnetic measurements.

**Key Achievements:**

- Biot-Savart Green's function derivation with Fourier-domain transfer function  $|\tilde{\mathcal{G}}(k)| = (\mu_0/2)e^{-kz_0}$
- Condition number scaling theorem:  $\kappa(\mathbf{G}_B) = e^{\pi z_0/\Delta x}$  limiting  $\Gamma_{\text{inv}}$
- Depth-amplitude ambiguity proof: why single-physics fails for  $d > 2z_0$
- Design rules linking standoff, resolution, SNR to reconstruction fidelity  $\Gamma_{\text{inv}} > 0.7$

**QFI Pipeline Position:**  $S(\mathbf{r}) \xrightarrow{\mathcal{G}} F(\mathbf{r}) \xrightarrow{\mathcal{M}} D \xrightarrow{\mathcal{R}} \hat{S}(\mathbf{r}) \pm \sigma_S$

### Abbreviated Terms

Abbreviation	Definition
BS	Biot-Savart
CRB	Cramér-Rao Bound
FA	Failure Analysis
FFT	Fast Fourier Transform
FIM	Fisher Information Matrix
FOV	Field of View
IC	Integrated Circuit
MTF	Modulation Transfer Function
NV	Nitrogen-Vacancy
OTF	Optical Transfer Function
PSF	Point Spread Function
QFI	Quantum Field Imaging
QFM	Quantum Field Metrology
Q-OTF	Quantum Optical Transfer Function
SNR	Signal-to-Noise Ratio
SVD	Singular Value Decomposition
TSV	Through-Silicon Via

### Abstract

This chapter develops the magnetic field forward model  $G_B$  that maps current density distributions  $\mathbf{J}(\mathbf{r})$  to measured magnetic fields  $\mathbf{B}(\mathbf{r})$ . Starting from the Biot-Savart law, we derive the Green's function formulation, analyze spatial decay characteristics, and establish the mathemat-

ical framework for discretization. The critical analysis of forward model conditioning reveals why magnetic-only reconstruction faces fundamental limits: the condition number  $\kappa(G_B)$  scales exponentially with the depth-to-stanoff ratio, limiting reconstruction fidelity to  $\Gamma_{\text{inv}} < 0.7$  for sources deeper than twice the stanoff distance. We prove the depth-amplitude ambiguity theorem, demonstrating that single-physics magnetic measurement cannot uniquely determine source depth and current magnitude simultaneously. This mathematical foundation motivates the multi-physics approaches developed in Chapter 11 and establishes quantitative design rules for QFI system specifications.

## 10.1 Introduction: Why Forward Models Matter

### 10.1.1 The Central Role of Forward Models in QFI

In the Quantum Field Imaging (QFI) framework established in Chapter 1, we introduced the operator stack that transforms hidden sources into reconstructed estimates:

$$S \xrightarrow{\mathcal{G}} F \xrightarrow{\mathcal{M}} D \xrightarrow{\mathcal{R}} \hat{S} \quad (10.1)$$

where  $S$  is the source distribution (e.g., current density),  $F$  is the physical field (e.g., magnetic field),  $D$  is the measured data, and  $\hat{S}$  is the reconstructed source estimate. The forward model  $\mathcal{G}$  occupies the critical first position in this chain, translating source physics into measurable fields.

This chapter focuses on the magnetic forward model  $\mathcal{G}_B$ , which describes how electric current distributions produce magnetic fields according to the Biot-Savart law. Understanding  $\mathcal{G}_B$  is essential because:

1. **Forward model accuracy determines  $\Gamma_{\text{mm}}$ :** Any mismatch between the assumed and true forward model directly degrades reconstruction fidelity through the model-mismatch penalty factor.
2. **Forward model conditioning determines  $\Gamma_{\text{inv}}$ :** The mathematical properties of  $\mathcal{G}_B$ —specifically its condition number—set fundamental limits on achievable reconstruction fidelity.
3. **Forward model structure guides algorithm design:** The sparsity, symmetry, and spectral properties of  $\mathcal{G}_B$  determine which reconstruction algorithms are efficient and stable.

### 10.1.2 Historical Background

The Biot-Savart law, formulated by Jean-Baptiste Biot and Félix Savart in 1820, describes the magnetic field generated by steady electric currents. For over two centuries, this fundamental relationship has underpinned:

- Classical magnetometry and compass design (19th century)
- Biomagnetism and magnetoencephalography (MEG) from the 1960s
- SQUID-based current imaging for IC failure analysis (1990s)
- NV-based wide-field magnetic microscopy (2010s–present)

The inverse problem—reconstructing current distributions from magnetic measurements—has been studied extensively in the MEG community, where it is known as the “magnetic inverse problem.” Key insights from this field, including the fundamental ill-posedness and depth ambiguity, directly inform QFI system design.

### 10.1.3 Pain Points in Current Practice

Practitioners attempting magnetic source reconstruction encounter several persistent challenges:

1. **Noise amplification:** Naïve inversion of magnetic data amplifies measurement noise, producing unphysical current reconstructions.
2. **Depth ambiguity:** A shallow, weak current produces the same magnetic signature as a deep, strong current, leading to non-unique solutions.
3. **Resolution degradation with depth:** Spatial features blur progressively for deeper sources, with no algorithmic remedy.
4. **Computational cost:** Direct matrix inversion for large images ( $> 1000 \times 1000$  pixels) becomes prohibitive without efficient algorithms.
5. **Boundary effects:** Finite measurement apertures introduce artifacts near image edges.

This chapter addresses each of these pain points through rigorous mathematical analysis and practical design rules.

### 10.1.4 Chapter Figures of Merit

Throughout this chapter, we track the following figures of merit:

Table 10.1: Key figures of merit for magnetic forward models

Metric	Symbol	Target	Units
Condition number	$\kappa(G_B)$	$< 10^4$	dimensionless
Reconstruction fidelity	$\Gamma_{\text{inv}}$	$> 0.85$	dimensionless
Model mismatch	$\Gamma_{\text{mm}}$	$> 0.95$	dimensionless
Spatial cutoff	$k_{\max}$	$> 1/\Delta x$	$\mu\text{m}^{-1}$
Computation time	$t_{\text{compute}}$	$< 100$ ms	ms per frame

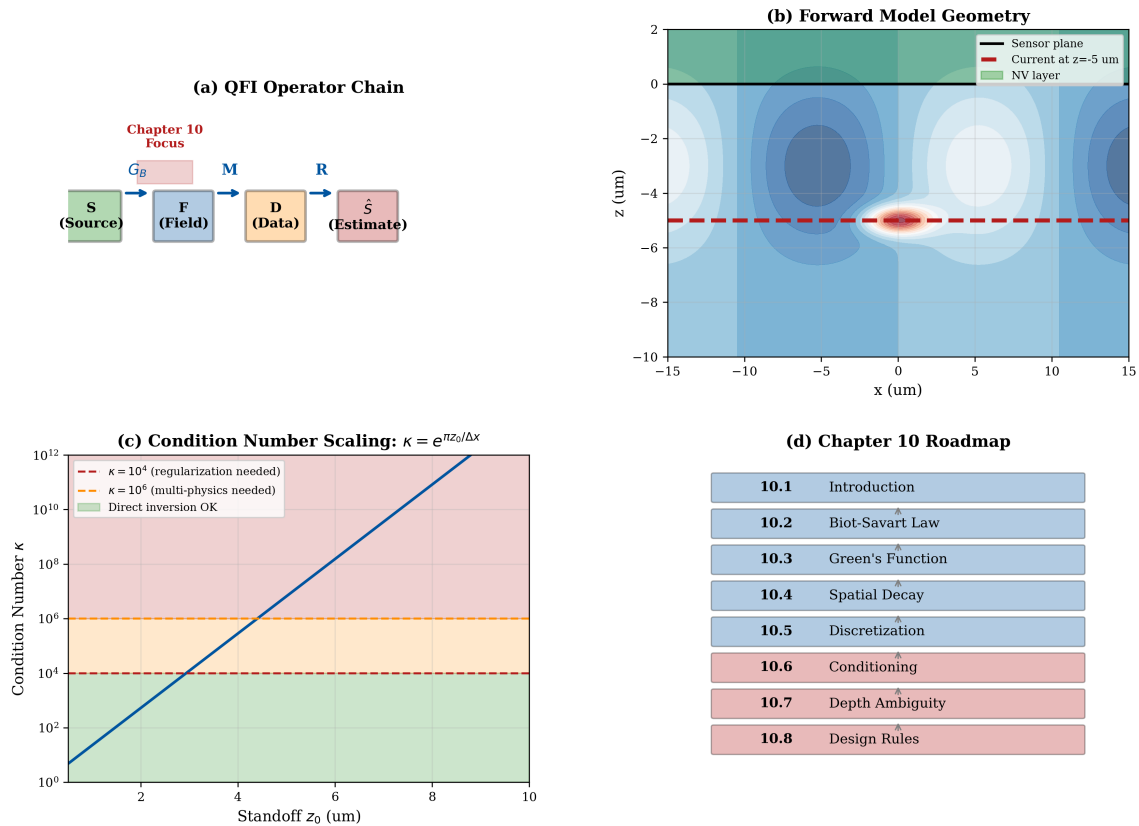


Figure 10.1: Chapter 10 overview: The magnetic forward model  $G_B$  bridges source currents to measured fields. (a) The QFI operator chain showing  $G_B$ 's central role. (b) Forward model maps current density  $J(x, y, z)$  to magnetic field  $B_z(x, y)$  at sensor plane. (c) Key challenge: the condition number  $\kappa(G_B)$  increases exponentially with depth, limiting reconstruction fidelity. (d) Chapter roadmap from Biot-Savart fundamentals through conditioning analysis to design rules.

## 10.2 The Biot-Savart Law: First Principles

### 10.2.1 Derivation from Maxwell's Equations

For steady currents ( $\partial\rho/\partial t = 0$ ), Ampère's law states:

$$\nabla \times \mathbf{B} = \mu_0 \mathbf{J} \quad (10.2)$$

where  $\mu_0 = 4\pi \times 10^{-7}$  T·m/A is the permeability of free space. Combined with the magnetic Gauss law  $\nabla \cdot \mathbf{B} = 0$ , we can express  $\mathbf{B}$  as the curl of a vector potential:

$$\mathbf{B} = \nabla \times \mathbf{A} \quad (10.3)$$

The vector potential satisfies the Poisson equation:

$$\nabla^2 \mathbf{A} = -\mu_0 \mathbf{J} \quad (10.4)$$

with solution:

$$\mathbf{A}(\mathbf{r}) = \frac{\mu_0}{4\pi} \int \frac{\mathbf{J}(\mathbf{r}')}{|\mathbf{r} - \mathbf{r}'|} dV' \quad (10.5)$$

Taking the curl yields the **Biot-Savart law**:

$$\boxed{\mathbf{B}(\mathbf{r}) = \frac{\mu_0}{4\pi} \int \frac{\mathbf{J}(\mathbf{r}') \times (\mathbf{r} - \mathbf{r}')}{|\mathbf{r} - \mathbf{r}'|^3} dV'} \quad (10.6)$$

This integral equation is the fundamental forward model for magnetic QFI: given any current distribution  $\mathbf{J}(\mathbf{r}')$ , we can compute the resulting magnetic field  $\mathbf{B}(\mathbf{r})$  at any observation point.

### 10.2.2 Physical Interpretation

The Biot-Savart law has several important physical features:

1. **Linearity:** The field  $\mathbf{B}$  depends linearly on the current  $\mathbf{J}$ . This enables superposition and linear algebraic treatment.
2.  **$1/r^2$  decay:** The kernel decays as  $1/|\mathbf{r} - \mathbf{r}'|^2$ , meaning distant sources contribute weakly to the local field.
3. **Vector cross product:** The field direction is perpendicular to both the current direction and the displacement vector, following the right-hand rule.
4. **Non-local dependence:** The field at any point depends on currents throughout the entire source volume—there is no “locality” in the forward problem.

### 10.2.3 Component Form for Planar Sources

For QFI applications, we typically measure the  $z$ -component of the magnetic field,  $B_z$ , at a planar sensor array located at height  $z = z_0$  above current sources in the  $z = 0$  plane. For a 2D current sheet  $\mathbf{J}(x', y') = J_x(x', y')\hat{x} + J_y(x', y')\hat{y}$ :

$$B_z(x, y, z_0) = \frac{\mu_0}{4\pi} \int \int \frac{J_x(x', y')(y - y') - J_y(x', y')(x - x')}{[(x - x')^2 + (y - y')^2 + z_0^2]^{3/2}} dx' dy' \quad (10.7)$$

This can be written as a convolution:

$$B_z(x, y) = G_{zx}(x, y, z_0) * J_x(x, y) + G_{zy}(x, y, z_0) * J_y(x, y) \quad (10.8)$$

where  $*$  denotes 2D convolution and  $G_{zx}$ ,  $G_{zy}$  are the Green's function kernels derived in the next section.

### 10.2.4 The Infinite Wire: A Canonical Example

Consider an infinite straight wire carrying current  $I$  along the  $x$ -axis at depth  $z = -d$  below the sensor plane. The Biot-Savart integral yields:

$$B_z(y) = \frac{\mu_0 I}{2\pi} \cdot \frac{d}{y^2 + d^2} \quad (10.9)$$

This result illustrates key features:

- Peak field occurs directly above the wire ( $y = 0$ ):  $B_z^{\max} = \mu_0 I / (2\pi d)$
- The field profile is a Lorentzian with half-width at half-maximum (HWHM) equal to  $d$
- Deeper wires produce broader, weaker signatures

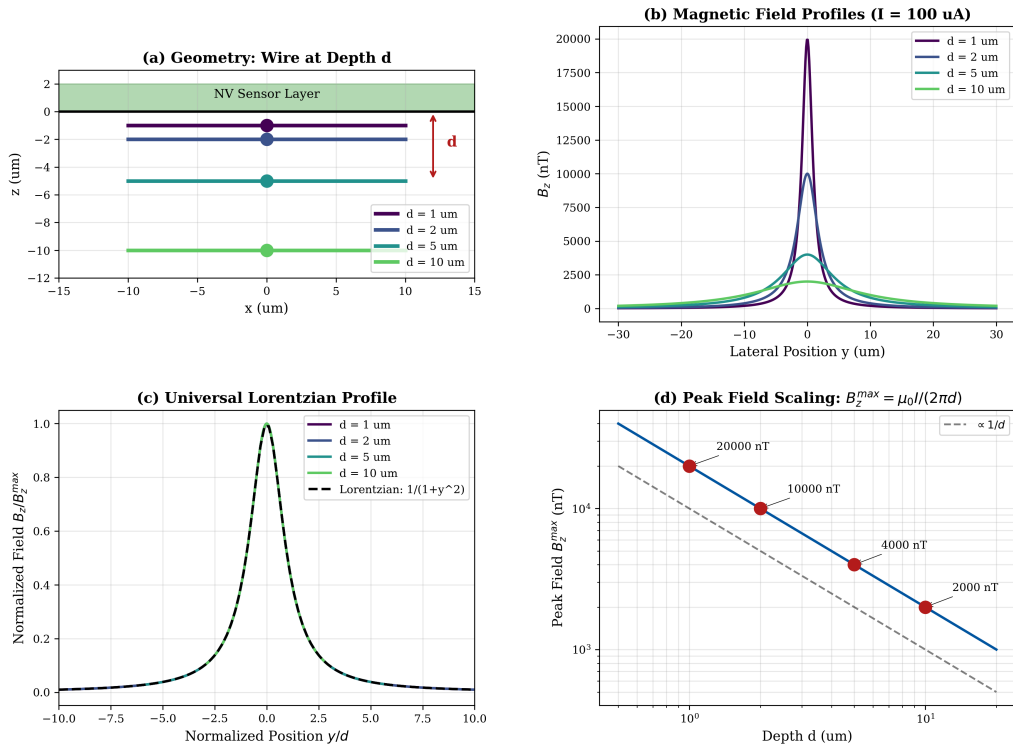


Figure 10.2: Magnetic field profiles from infinite wires at different depths. (a) Geometry showing wire at depth  $d$  below sensor plane. (b)  $B_z$  profiles for  $d = 1, 2, 5, 10 \mu\text{m}$  with  $I = 100 \mu\text{A}$ . Deeper wires produce broader, weaker signatures. (c) Normalized profiles collapse to universal Lorentzian shape when scaled by depth. (d) Peak field vs. depth showing  $1/d$  scaling.

## 10.3 Green's Function Formulation

### 10.3.1 Definition and Properties

The Green's function  $G(\mathbf{r}, \mathbf{r}')$  is the magnetic field at  $\mathbf{r}$  due to a unit point current at  $\mathbf{r}'$ . For the Biot-Savart law, the Green's function tensor is:

$$G_{ij}(\mathbf{r}, \mathbf{r}') = \frac{\mu_0}{4\pi} \cdot \frac{\epsilon_{ijk}(r_k - r'_k)}{|\mathbf{r} - \mathbf{r}'|^3} \quad (10.10)$$

where  $\epsilon_{ijk}$  is the Levi-Civita symbol.

For the  $z$ -component measured at height  $z_0$  from currents at  $z = 0$ :

$$G_{zx}(x, y, z_0) = \frac{\mu_0}{4\pi} \cdot \frac{y}{(x^2 + y^2 + z_0^2)^{3/2}} \quad (10.11)$$

$$G_{zy}(x, y, z_0) = -\frac{\mu_0}{4\pi} \cdot \frac{x}{(x^2 + y^2 + z_0^2)^{3/2}} \quad (10.12)$$

### 10.3.2 Fourier Domain Representation

The convolution form of the forward model becomes multiplication in Fourier space. Taking the 2D Fourier transform:

$$\tilde{B}_z(k_x, k_y) = \tilde{G}_{zx}(k_x, k_y, z_0)\tilde{J}_x(k_x, k_y) + \tilde{G}_{zy}(k_x, k_y, z_0)\tilde{J}_y(k_x, k_y) \quad (10.13)$$

The Fourier-space Green's functions are:

$$\tilde{G}_{zx}(k_x, k_y, z_0) = \frac{\mu_0}{2} \cdot \frac{ik_y}{k} \cdot e^{-kz_0} \quad (10.14)$$

$$\tilde{G}_{zy}(k_x, k_y, z_0) = -\frac{\mu_0}{2} \cdot \frac{ik_x}{k} \cdot e^{-kz_0} \quad (10.15)$$

where  $k = \sqrt{k_x^2 + k_y^2}$  is the radial spatial frequency.

The magnitude of the magnetic transfer function is:

$$|\tilde{G}_B(k, z_0)| = \frac{\mu_0}{2} e^{-kz_0} \quad (10.16)$$

This exponential decay with spatial frequency is the fundamental cause of ill-conditioning in magnetic reconstruction.

### 10.3.3 Physical Interpretation of Exponential Decay

The exponential factor  $e^{-kz_0}$  has profound implications:

1. **Low-pass filtering:** High spatial frequencies (small features) are exponentially attenuated with standoff distance.
2. **Resolution limit:** Features smaller than approximately  $z_0$  are strongly suppressed in the measured field.
3. **Information loss:** The exponential decay means information about fine source details is effectively lost—no amount of post-processing can recover it without additional measurements.

The magnetic forward model acts as a low-pass filter with characteristic cutoff  $k_c \approx 1/z_0$ . To resolve features of size  $\Delta x$ , the standoff must satisfy  $z_0 < \Delta x$ . This is fundamentally different from optical resolution limits (which depend on wavelength) and cannot be improved by better sensors or algorithms.

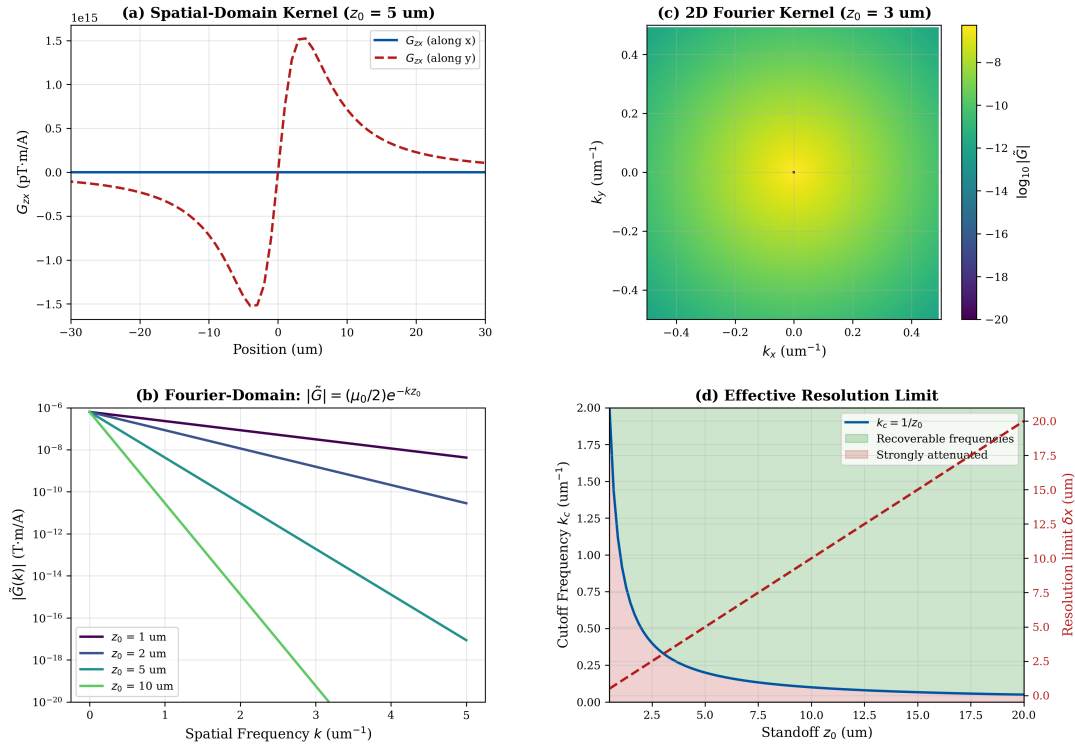


Figure 10.3: Green’s function analysis. (a) Spatial-domain kernels  $G_{zx}$  and  $G_{zy}$  showing antisymmetric structure. (b) Fourier-domain magnitude  $|\tilde{G}_B(k)|$  for different standoff distances, showing exponential decay. (c) Phase of Fourier kernel showing  $\pi/2$  shift between components. (d) Effective cutoff frequency  $k_c = 1/z_0$  vs. standoff distance.

## 10.4 Spatial Decay Analysis

### 10.4.1 Near-Field vs. Far-Field Regimes

The magnetic field decay with distance exhibits two distinct regimes:

**Near-field** ( $r \ll \text{source size}$ ): The field decays as  $1/r^2$  and retains detailed information about source structure.

**Far-field** ( $r \gg \text{source size}$ ): The field decays as  $1/r^3$  (dipole regime) and source details are lost.

For QFI applications with typical standoff distances of 1–10  $\mu\text{m}$  and source features of similar scale, we operate in the **near-field regime**.

### 10.4.2 Decay Scaling Laws

For a localized current source of characteristic size  $a$  at depth  $d$ :

Table 10.2: Magnetic field scaling in different regimes

Regime	Condition	Field Scaling
Contact	$d \ll a$	$B \sim \mu_0 J$
Near-field	$d \sim a$	$B \sim \mu_0 I a / d^2$
Far-field (dipole)	$d \gg a$	$B \sim \mu_0 I a^2 / d^3$

### 10.4.3 Depth-Dependent Resolution

The minimum resolvable lateral feature size  $\delta x_{\min}$  depends on depth  $d$  and signal-to-noise ratio:

$$\delta x_{\min}(d) \approx \frac{d}{\sqrt{\text{SNR}}} \quad (10.17)$$

**Theorem 10.4.1** (Depth-Resolution Theorem). *For a QFI system with measurement noise  $\sigma_B$  and current sensitivity  $\delta J_{\min}$ , the minimum resolvable feature size at depth  $d$  is:*

$$\delta x_{\min} = d \cdot \sqrt{\frac{\sigma_B}{\mu_0 \delta J_{\min} / (2\pi)}} \quad (10.18)$$

*Proof.* The magnetic field from a feature of size  $\delta x$  carrying current density  $J$  at depth  $d$  scales as  $B \sim \mu_0 J \delta x^2 / (2\pi d^2)$  in the near-field. Setting  $B = \sigma_B$  (minimum detectable) and solving for  $\delta x$  yields the result.  $\square$

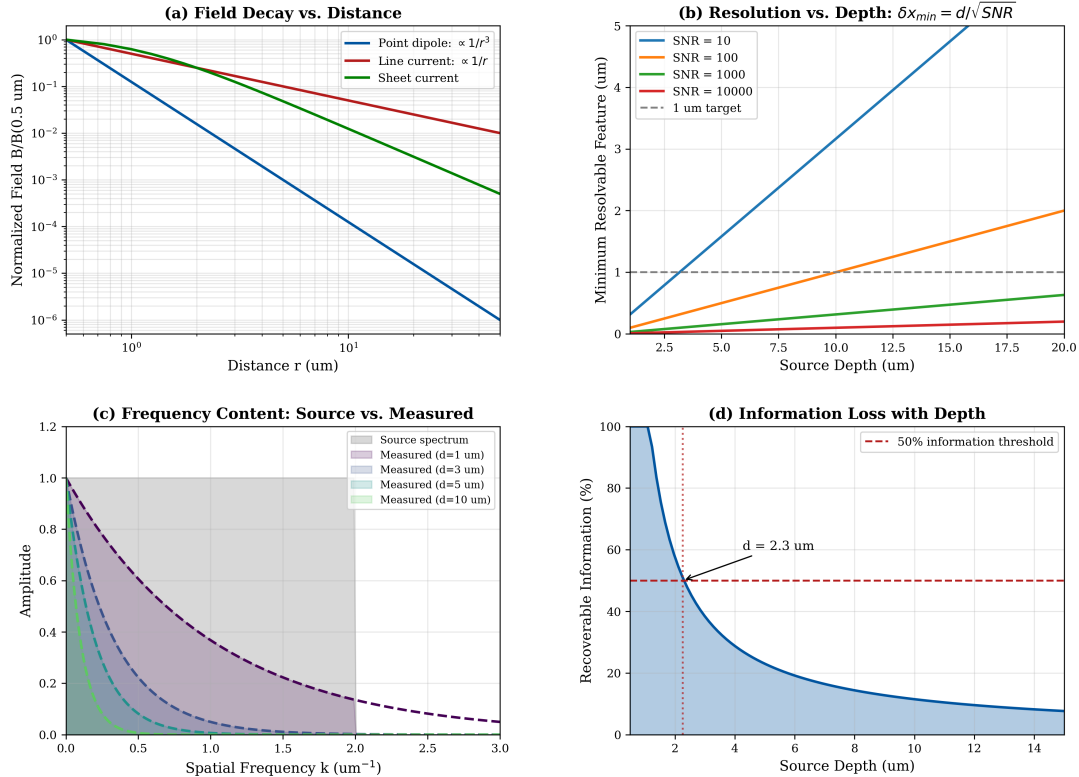


Figure 10.4: Spatial decay analysis. (a) Field decay curves for point dipole, line current, and sheet current showing different power laws. (b) Resolution vs. depth for different SNR values. (c) Spatial frequency content of measured field vs. source at different depths. (d) Information loss quantified as recoverable spatial frequency bandwidth.

## 10.5 Discretization and Matrix Form

### 10.5.1 Voxel-Based Discretization

For computational implementation, we discretize the source region into  $n$  voxels with positions  $\{\mathbf{r}'_j\}_{j=1}^n$  and the measurement region into  $m$  pixels with positions  $\{\mathbf{r}_i\}_{i=1}^m$ . The continuous forward model becomes:

$$B_i = \sum_{j=1}^n G_{ij} J_j + \epsilon_i \quad (10.19)$$

In matrix form:

$$\mathbf{b} = \mathbf{G}\mathbf{j} + \boldsymbol{\epsilon} \quad (10.20)$$

where  $\mathbf{G} \in \mathbb{R}^{m \times n}$  is the forward matrix with elements:

$$G_{ij} = G(\mathbf{r}_i, \mathbf{r}'_j) \cdot \Delta V_j \quad (10.21)$$

and  $\Delta V_j$  is the voxel volume.

### 10.5.2 Matrix Structure and Sparsity

The forward matrix  $\mathbf{G}$  has several important structural properties:

1. **Dense:** Every source voxel contributes to every measurement pixel (no strict sparsity).
2. **Toeplitz-like:** For regular grids,  $\mathbf{G}$  has block-Toeplitz structure enabling FFT-based multiplication.
3. **Low-rank approximation:** The rapid decay of singular values allows efficient low-rank approximations.
4. **Shift-invariant:** The kernel depends only on  $\mathbf{r} - \mathbf{r}'$ , not on absolute position (except near boundaries).

### 10.5.3 FFT-Based Implementation

For shift-invariant systems on regular grids, the matrix-vector product  $\mathbf{G}\mathbf{j}$  can be computed efficiently via FFT:

$$\mathbf{b} = \mathcal{F}^{-1} \left[ \tilde{\mathbf{G}} \odot \mathcal{F}[\mathbf{j}] \right] \quad (10.22)$$

where  $\mathcal{F}$  denotes the FFT,  $\tilde{\mathbf{G}}$  is the pre-computed Fourier-domain kernel, and  $\odot$  is element-wise multiplication.

Table 10.3: Computational complexity comparison

Method	Forward	Memory
Direct matrix	$O(mn)$	$O(mn)$
FFT-based	$O(n \log n)$	$O(n)$
Hierarchical (FMM)	$O(n)$	$O(n)$

For a  $1000 \times 1000$  pixel image, FFT-based methods provide  $\sim 10^6 \times$  speedup over direct matrix multiplication.

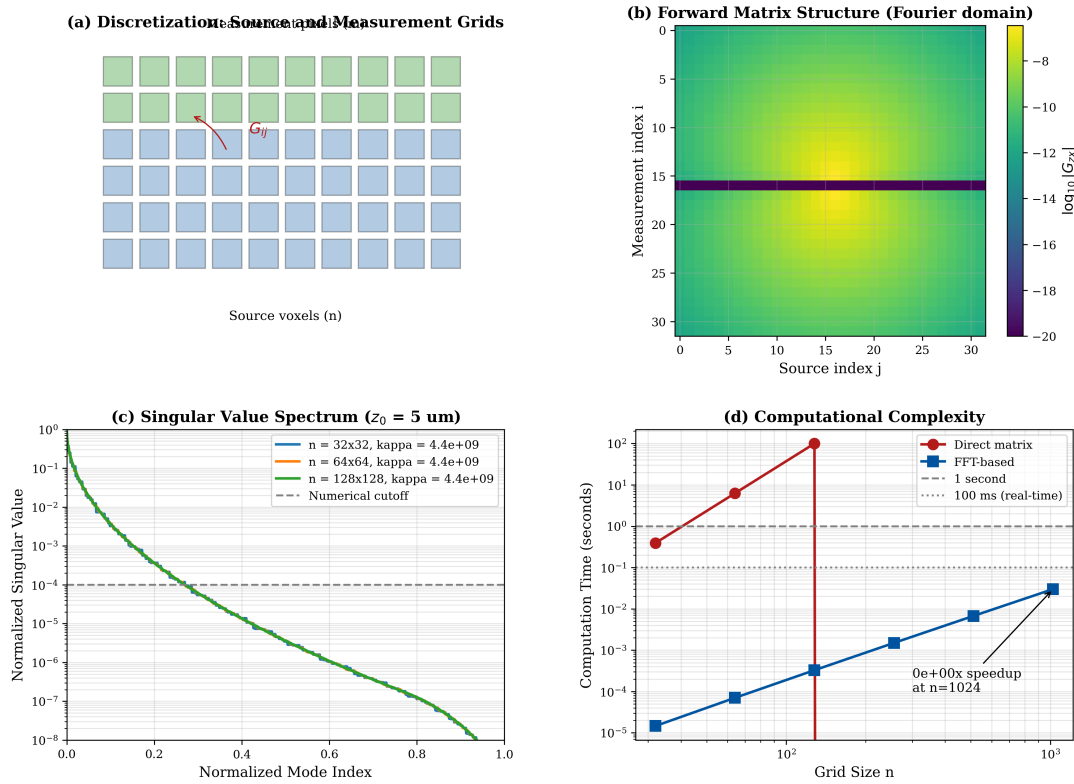


Figure 10.5: Discretization and matrix structure. (a) Voxel grid for source region and pixel grid for measurement. (b) Forward matrix structure showing block-Toeplitz pattern. (c) Singular value spectrum of  $\mathbf{G}$  showing exponential decay. (d) Computation time comparison: direct vs. FFT methods.

#### Implementation Note: FFT-Based Forward Model Recipe

**Step 1: Zero-padding.** Pad both source and measurement grids to at least  $2N \times 2N$  (factor of 2 in each dimension) to convert circular convolution to linear convolution and suppress wrap-around artifacts.

**Step 2: Kernel precomputation.** Compute the Fourier-domain kernel  $\tilde{G}(k_x, k_y)$  once on the padded grid. Set  $\tilde{G}(0, 0) = 0$  to exclude the DC mode (see Section 10.5.4).

**Step 3: Forward evaluation.** The forward model is:

$$\mathbf{b} = \text{IFFT}[\tilde{G} \cdot \text{FFT}[\mathbf{j}]]$$

Crop the result to the original  $N \times N$  measurement grid.

**Step 4: Boundary mitigation.** For sources near the FOV edge, apply a raised-cosine (Tukey) window with taper ratio 0.1–0.2 to suppress Gibbs ringing. Alternatively, use mirror-symmetric boundary extension if the source geometry permits.

**Computational cost:**  $\mathcal{O}(N^2 \log N)$  per forward evaluation, versus  $\mathcal{O}(N^4)$  for direct matrix–vector product.

#### 10.5.4 Identifiability Constraints and the DC Mode

The Fourier-domain forward kernels (Equations 10.14–10.15) contain factors of the form  $ik_x/k$  and  $ik_y/k$ , which are singular at  $k = 0$ . This singularity reflects a genuine physical subtlety that affects both the mathematical formulation and practical FFT implementation.

**What is measured.** Most NV-based QFI systems measure only the  $B_z$  component (projection along the NV axis). For the scalar  $B_z$  from a 2D current sheet, the Fourier-domain forward model takes the simpler form:

$$\tilde{B}_z(k_x, k_y) = \frac{\mu_0}{2} e^{-kz_0} \frac{ik_x \tilde{J}_y(k_x, k_y) - ik_y \tilde{J}_x(k_x, k_y)}{k} \quad (10.23)$$

where  $k = \sqrt{k_x^2 + k_y^2}$ . At  $k = 0$ , this expression is 0/0—indeterminate—because a spatially uniform current produces no net  $B_z$  at the sensor plane (by symmetry).

**Current conservation constraint.** For steady-state currents in IC metallization, charge conservation requires  $\nabla \cdot \mathbf{J} = 0$ , i.e., in Fourier space:

$$k_x \tilde{J}_x + k_y \tilde{J}_y = 0 \quad (10.24)$$

This constraint eliminates one degree of freedom: the current can be parameterized by a scalar **stream function**  $\psi(x, y)$  with  $J_x = \partial\psi/\partial y$ ,  $J_y = -\partial\psi/\partial x$ , reducing the unknowns from two components ( $J_x, J_y$ ) to one scalar field  $\psi$ .

**Practical DC handling in FFT implementation.** For the discrete FFT-based forward model, the  $k = 0$  mode should be handled explicitly:

1. **Set  $\tilde{G}(0, 0) = 0$ :** The DC component of  $B_z$  carries no information about the current structure; exclude it from the forward model.
2. **Apply the divergence-free constraint:** Parameterize  $\mathbf{J}$  via the stream function  $\psi$  when current conservation holds (steady-state IC currents). This eliminates the  $k = 0$  singularity and halves the unknown count from  $2N^2$  to  $N^2$ .
3. **Distinguish rank deficiency from ill-conditioning:** The  $k = 0$  mode is a true null-space direction (rank deficiency), whereas high- $k$  modes are merely ill-conditioned. Regularization addresses the latter but not the former; the DC mode must be removed or constrained explicitly.

#### Implementation Note: Stream Function for IC Currents

For divergence-free currents ( $\nabla \cdot \mathbf{J} = 0$ ), the stream function formulation  $J_x = \partial\psi/\partial y$ ,  $J_y = -\partial\psi/\partial x$  yields a scalar forward model:

$$\tilde{B}_z(\mathbf{k}) = \frac{\mu_0}{2} k e^{-kz_0} \tilde{\psi}(\mathbf{k}) \quad (10.25)$$

This formulation (i) eliminates the  $k = 0$  singularity since  $k \cdot e^{-kz_0} \rightarrow 0$  as  $k \rightarrow 0$ , (ii) reduces the problem to a scalar inversion, and (iii) automatically enforces current conservation. It is the recommended formulation for IC failure analysis applications.

## 10.6 Conditioning Analysis

### 10.6.1 Singular Value Decomposition

The forward matrix  $\mathbf{G}$  admits the singular value decomposition (SVD):

$$\mathbf{G} = \mathbf{U} \boldsymbol{\Sigma} \mathbf{V}^T = \sum_{i=1}^r \sigma_i \mathbf{u}_i \mathbf{v}_i^T \quad (10.26)$$

where  $\sigma_1 \geq \sigma_2 \geq \dots \geq \sigma_r > 0$  are the singular values, and  $r = \text{rank}(\mathbf{G})$ .

### 10.6.2 Condition Number Definition

The **condition number** quantifies the sensitivity of the inverse problem to perturbations:

**Definition 10.6.1** (Condition Number). The condition number of matrix  $\mathbf{G}$  is:

$$\kappa(\mathbf{G}) = \frac{\sigma_{\max}}{\sigma_{\min}} = \frac{\sigma_1}{\sigma_r} \quad (10.27)$$

For the naive inverse  $\hat{\mathbf{j}} = \mathbf{G}^{-1}\mathbf{b}$ , measurement noise  $\epsilon$  is amplified by:

$$\|\hat{\mathbf{j}} - \mathbf{j}\| \leq \kappa(\mathbf{G}) \cdot \frac{\|\epsilon\|}{\|\mathbf{b}\|} \quad (10.28)$$

### 10.6.3 Condition Number Scaling Theorem

#### 10.6.3.1 Condition Number Scaling Theorem

Before stating the scaling law, we establish spatial frequency conventions used throughout this chapter and the remainder of the book.

##### Frequency Conventions

All spatial frequencies in this chapter are *angular* spatial frequencies in units of rad/ $\mu\text{m}$ :

- 1D Nyquist frequency along one axis:  $k_{\text{Nyq}} = \pi/\Delta x$
- 2D Nyquist corner (diagonal of the Nyquist square):  $k_{\text{corner}} = \sqrt{2}\pi/\Delta x$
- Radial Nyquist (circular band-limit):  $k_{\max} = \pi/\Delta x$  (conservative; used in design rules)

The condition number depends on which  $k_{\max}$  is adopted. We present both the **1D/axial bound** (typical case) and the **2D corner bound** (worst case).

**Theorem 10.6.1** (Condition Number Scaling—1D Axial Bound). *For the Biot-Savart forward model with standoff  $z_0$  and grid spacing  $\Delta x$ , evaluated along a single Fourier axis, the condition number is:*

$$\kappa_{1D}(G) = e^{\pi z_0/\Delta x} \quad (10.29)$$

*Proof.* In Fourier space the singular values of  $G$  are proportional to  $|\tilde{G}(k)| = (\mu_0/2) e^{-kz_0}$ . The maximum occurs at  $k = 0$ :

$$\sigma_{\max} \propto \frac{\mu_0}{2} \quad (10.30)$$

The minimum along one axis occurs at  $k_{\text{Nyq}} = \pi/\Delta x$ :

$$\sigma_{\min}^{(1D)} \propto \frac{\mu_0}{2} e^{-\pi z_0/\Delta x} \quad (10.31)$$

Therefore  $\kappa_{1D} = \sigma_{\max}/\sigma_{\min}^{(1D)} = e^{\pi z_0/\Delta x}$ . □

**Corollary 10.6.1** (2D Nyquist Corner Bound). *For the 2D problem on a square grid, the worst-case condition number (at the Nyquist corner  $k = \sqrt{2}\pi/\Delta x$ ) is:*

$$\kappa_{2D}(G) = e^{\sqrt{2}\pi z_0/\Delta x} \quad (10.32)$$

*This is the conservative (worst-case) bound applicable to 2D reconstruction.*

*Remark 10.6.1.* The ratio  $\kappa_{2D}/\kappa_{1D} = e^{(\sqrt{2}-1)\pi z_0/\Delta x}$  grows rapidly with  $z_0/\Delta x$ . For  $z_0/\Delta x = 3$ :  $\kappa_{1D} \approx 1.2 \times 10^4$  while  $\kappa_{2D} \approx 6 \times 10^5$ —a factor of  $\sim 50$ . Design rules in this chapter use the 1D bound (Equation 10.29) as the **typical operating bound**, with the 2D corner (Equation 10.32) reserved as the **worst-case bound** for conservative system specification.

**Typical (1D axial):**

$$\kappa_{1D}(G_B) = e^{\pi z_0/\Delta x} \quad (10.33)$$

**Worst-case (2D corner):**

$$\kappa_{2D}(G_B) = e^{\sqrt{2}\pi z_0/\Delta x} \quad (10.34)$$

For  $z_0 = 5 \mu\text{m}$  and  $\Delta x = 1 \mu\text{m}$ :  $\kappa_{1D} = e^{5\pi} \approx 5 \times 10^6$ ;  $\kappa_{2D} = e^{5\sqrt{2}\pi} \approx 3 \times 10^9$ .

#### 10.6.4 Implications for Reconstruction Fidelity

The condition number provides an engineering proxy for the achievable reconstruction fidelity  $\Gamma_{\text{inv}}$ . We derive this proxy under explicit assumptions.

**Derivation sketch.** Consider the linear inverse estimate  $\hat{\mathbf{j}} = G^{-1}\mathbf{b}$  where  $\mathbf{b} = G\mathbf{j} + \boldsymbol{\epsilon}$  with white Gaussian noise  $\boldsymbol{\epsilon} \sim \mathcal{N}(0, \sigma^2 I)$ . The reconstruction error is:

$$\hat{\mathbf{j}} - \mathbf{j} = G^{-1}\boldsymbol{\epsilon} \quad (10.35)$$

The expected relative error, averaged over noise realizations, satisfies:

$$\frac{\mathbb{E}\|\hat{\mathbf{j}} - \mathbf{j}\|^2}{\|\mathbf{j}\|^2} \leq \frac{\kappa(G)^2}{\text{SNR}^2} \quad (\text{worst case}) \quad (10.36)$$

Defining reconstruction fidelity as  $\Gamma_{\text{inv}} = 1 - \text{NRMSE}$  and using the root-mean-square average (rather than worst-case) yields the **design-stage proxy**:

#### Design Proxy: Reconstruction Fidelity Bound

Under the assumptions of (1) an unregularized linear estimator, (2) additive white Gaussian noise, and (3) worst-case source alignment with the minimum singular vector:

$$\Gamma_{\text{inv}}^{\text{proxy}} \leq \frac{1}{1 + \kappa(G)/\text{SNR}} \quad (10.37)$$

This is a **conservative design proxy**, not a tight bound. With regularization (Tikhonov, TV,  $\ell_1$ ), the actual  $\Gamma_{\text{inv}}$  can exceed this proxy significantly—see Chapter 14 for regularized reconstruction analysis.

*Remark 10.6.2.* The proxy  $\Gamma_{\text{inv}}^{\text{proxy}}$  is most useful at the system design stage, where it provides a quick check on whether a given  $(z_0, \Delta x, \text{SNR})$  combination is viable *before* committing to detailed reconstruction algorithm development. For production performance prediction, use the regularized fidelity metrics developed in Chapter 14.

Table 10.4: Condition number and proxy reconstruction fidelity  $\Gamma_{\text{inv}}^{\text{proxy}}$  (Equation 10.37) for typical parameters. Regularized reconstruction (Chapter 14) can achieve fidelity above these proxy values.

$z_0/\Delta x$	$\kappa(\mathbf{G})$	$\Gamma_{\text{inv}}$ (SNR=100)	$\Gamma_{\text{inv}}$ (SNR=1000)
1	$2.3 \times 10^1$	0.81	0.98
2	$5.4 \times 10^2$	0.16	0.65
3	$1.2 \times 10^4$	0.008	0.08
5	$5.4 \times 10^6$	< 0.001	0.0002

For stable reconstruction with  $\Gamma_{\text{inv}} > 0.7$ , the standoff distance must satisfy:

$$z_0 < \frac{\ln(\text{SNR})}{\pi} \cdot \Delta x \approx 1.5\Delta x \quad \text{for SNR} = 100 \quad (10.38)$$

To resolve 1  $\mu\text{m}$  features with  $\Gamma_{\text{inv}} > 0.7$ , standoff must be  $z_0 < 1.5 \mu\text{m}$ .

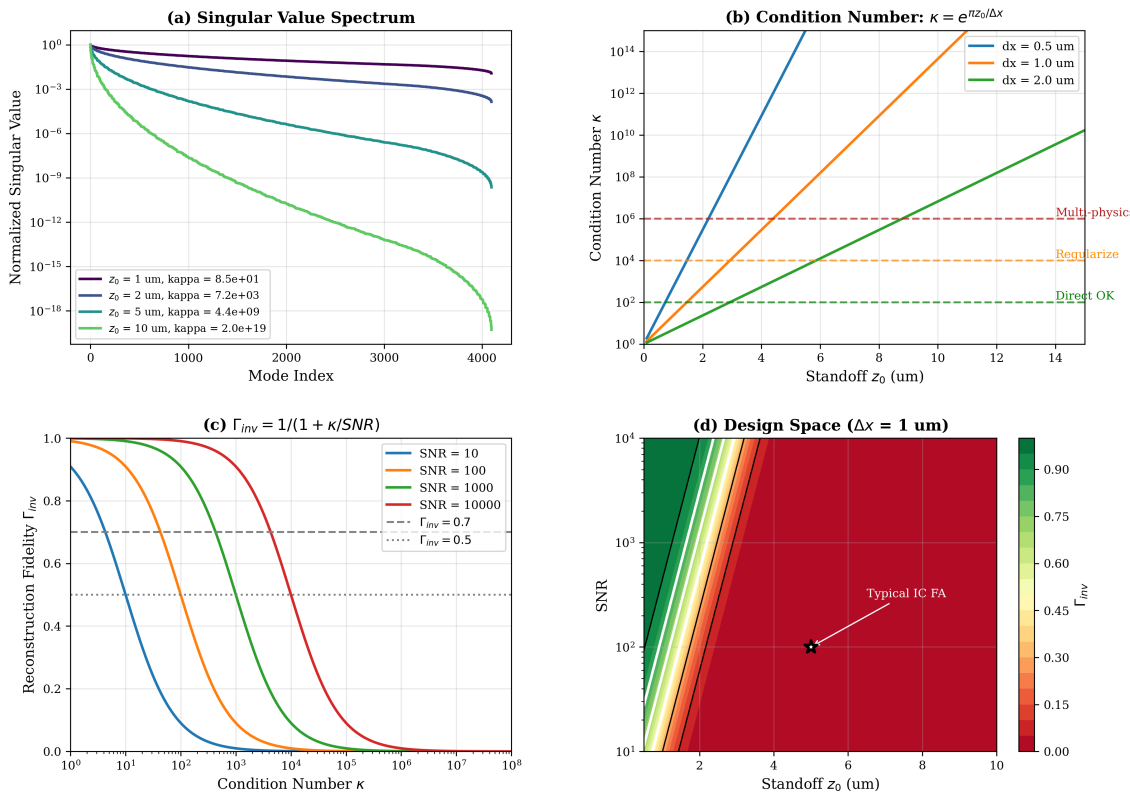


Figure 10.6: Conditioning analysis of the Biot-Savart forward model. (a) Singular value spectrum showing exponential decay with mode index. (b) Condition number vs. standoff distance (log scale); curves correspond to the 1D axial bound  $\kappa_{1D}$  (Theorem 10.6.1). The 2D corner bound (Corollary 10.6.1) is  $\sqrt{2}\times$  steeper on a log scale. (c) Proxy reconstruction fidelity  $\Gamma_{\text{inv}}^{\text{proxy}}$  (Equation 10.37) vs. condition number for different SNR values; actual  $\Gamma_{\text{inv}}$  with regularization can exceed these values. (d) Design space showing acceptable operating region ( $\Gamma_{\text{inv}} > 0.7$ ).

## 10.7 Depth-Amplitude Ambiguity: Why Single-Physics Fails

### 10.7.1 The Fundamental Non-Identifiability

A critical limitation of magnetic-only measurement is the **depth-amplitude ambiguity**: for band-limited, noisy, single-plane measurements, different combinations of current magnitude and source depth produce statistically indistinguishable magnetic signatures. This is not an engineering limitation that better hardware can overcome—it is a structural property of the magnetic forward model.

**Theorem 10.7.1** (Depth-Amplitude Non-Identifiability). *Consider a localized current source characterized by parameters  $(I, d)$  (current magnitude and depth), measured via single-plane  $B_z(x, y)$  with additive noise of variance  $\sigma_B^2$  and band-limited to spatial frequencies  $|k| \leq k_{\max}$ .*

**(i) Scaling property.** *The transformation  $(I, d) \rightarrow (\alpha^2 I, \alpha d)$  produces a magnetic signature that differs from the original by a global scale factor  $\alpha$  in both amplitude and spatial extent:*

$$B'_z(x, y) = \alpha \cdot B_z(x/\alpha, y/\alpha) \quad (10.39)$$

**(ii) Non-identifiability.** *For measurement noise level  $\sigma_B$  and band-limited spatial frequency content  $k \leq k_{\max}$ , there exists a connected **ambiguity manifold***

$$\mathcal{M}_\delta = \{(I', d') : \|\mathbf{B}_{\text{meas}} - \mathbf{B}_{\text{model}}(I', d')\|_2 < \delta\} \quad (10.40)$$

*of dimension  $\geq 1$  in the  $(I, d)$  parameter space, where  $\delta = \sigma_B \sqrt{N_{\text{pix}}}$  is the noise floor. The manifold width grows with increasing source depth.*

*Proof.* **Part (i):** For a wire at depth  $d$  carrying current  $I$ , the Biot-Savart law gives:

$$B_z(y) = \frac{\mu_0 I}{2\pi} \cdot \frac{d}{y^2 + d^2} \quad (10.41)$$

with peak field  $B_z^{\max} = \mu_0 I / (2\pi d)$  and half-width  $w = d$ . Under the transformation  $(I, d) \rightarrow (\alpha^2 I, \alpha d)$ :

$$B'^{\max}_z = \frac{\mu_0(\alpha^2 I)}{2\pi(\alpha d)} = \alpha \cdot B_z^{\max} \quad (10.42)$$

$$w' = \alpha d = \alpha \cdot w \quad (10.43)$$

Both the peak field and spatial width scale by  $\alpha$ , confirming Equation (10.39). The two signatures are *not identical*—they differ by the global factor  $\alpha$ .

**Part (ii):** Although the signatures are not strictly invariant, they become *statistically indistinguishable* under realistic measurement conditions. In the Fourier domain, the band-limited measurement retains only  $|k| \leq k_{\max}$ . The residual between the true source  $(I, d)$  and a candidate  $(\alpha^2 I, \alpha d)$  is:

$$R(\alpha) = \sum_{|k| \leq k_{\max}} |\tilde{B}_z(k) - \alpha \tilde{B}_z(k/\alpha)|^2 \quad (10.44)$$

For  $|\alpha - 1| < \epsilon$  with  $\epsilon \ll 1$ , a Taylor expansion gives  $R(\alpha) \propto (\alpha - 1)^2 \cdot \sigma_k^2$ , where  $\sigma_k^2 = \sum k^2 |\tilde{B}_z(k)|^2$  is the spectral second moment. Because the exponential decay  $|\tilde{G}(k)| \propto e^{-kd}$  suppresses high- $k$  content for deep sources,  $\sigma_k^2$  decreases with depth, making  $R(\alpha) < \delta^2$  over a wider range of  $\alpha$ . Hence the manifold  $\mathcal{M}_\delta$  broadens as  $d$  increases.

More precisely, the Fisher Information Matrix for parameters  $(I, d)$  has off-diagonal elements whose magnitude grows relative to the diagonal as  $d$  increases. The correlation coefficient  $\rho_{Id} = [\mathbf{J}^{-1}]_{12} / \sqrt{[\mathbf{J}^{-1}]_{11} [\mathbf{J}^{-1}]_{22}}$  approaches  $|\rho_{Id}| \rightarrow 1$  for  $d \gg \Delta x$ , confirming that the two parameters become practically non-identifiable.  $\square$

*Remark 10.7.1* (Scope of the Ambiguity). The non-identifiability theorem applies specifically to:

1. **Geometry:** Localized sources (wires, compact current paths). For spatially extended sources with known structure (e.g., CAD-informed IC layouts), prior information partially constrains the manifold.
2. **Measurement:** Single-plane  $B_z$  measurements. Multi-plane sensing (Section 7.8.4) reduces the ambiguity by providing depth discrimination.
3. **Physics:** Magnetic-only sensing. Multi-physics measurements (Chapter 11) break the ambiguity because the thermal signature scales as  $\Delta T \propto I^2 R$  (nonlinear in  $I$ ), which is inconsistent with the linear scaling of the magnetic signature.

*Remark 10.7.2* (Relation to Chapter 7 Scaling Law). Theorem 7.8.1 presents a different scaling law  $\alpha(z) = (z/z_0)^3$  for the depth-current ambiguity. The distinction is the source model: Chapter 7 treats volumetric current distributions integrated over depth (3D ambiguity), while Theorem 10.7.1 treats localized sources at a single depth (2D parameter ambiguity). Both express the same underlying physics—exponential information loss with depth—in different geometric settings. Table 10.5 summarizes the relationship.

Table 10.5: Comparison of depth-amplitude ambiguity formulations across chapters

Property	Thm. 7.8.1 (Ch. 7)	Thm. 10.7.1 (Ch. 10)	Ch. 2 (Eq. 2.51)
Source model	Volumetric $J(x, y, z)$	Localized wire $(I, d)$	Sheet current $B_0 f(x/z)$
Scaling law	$\alpha(z) = (z/z_0)^3$	$(I, d) \rightarrow (\alpha^2 I, \alpha d)$	$I \rightarrow 4I, d \rightarrow 2d$
Ambiguity type	Depth-integrated	Parametric manifold	Profile degeneracy
Resolution	Multi-plane sensing	Multi-physics	Multi-physics

## 10.7.2 Mathematical Formulation of Ambiguity

The ambiguity can be formalized through the null space of the Hessian. Define the residual:

$$R(I, d) = \|B_{\text{meas}} - B_{\text{model}}(I, d)\|^2 \quad (10.45)$$

The ambiguity manifold is defined by  $R(I, d) = R_{\min}$ . For magnetic-only measurements, this manifold is not a single point but a curve in  $(I, d)$  space.

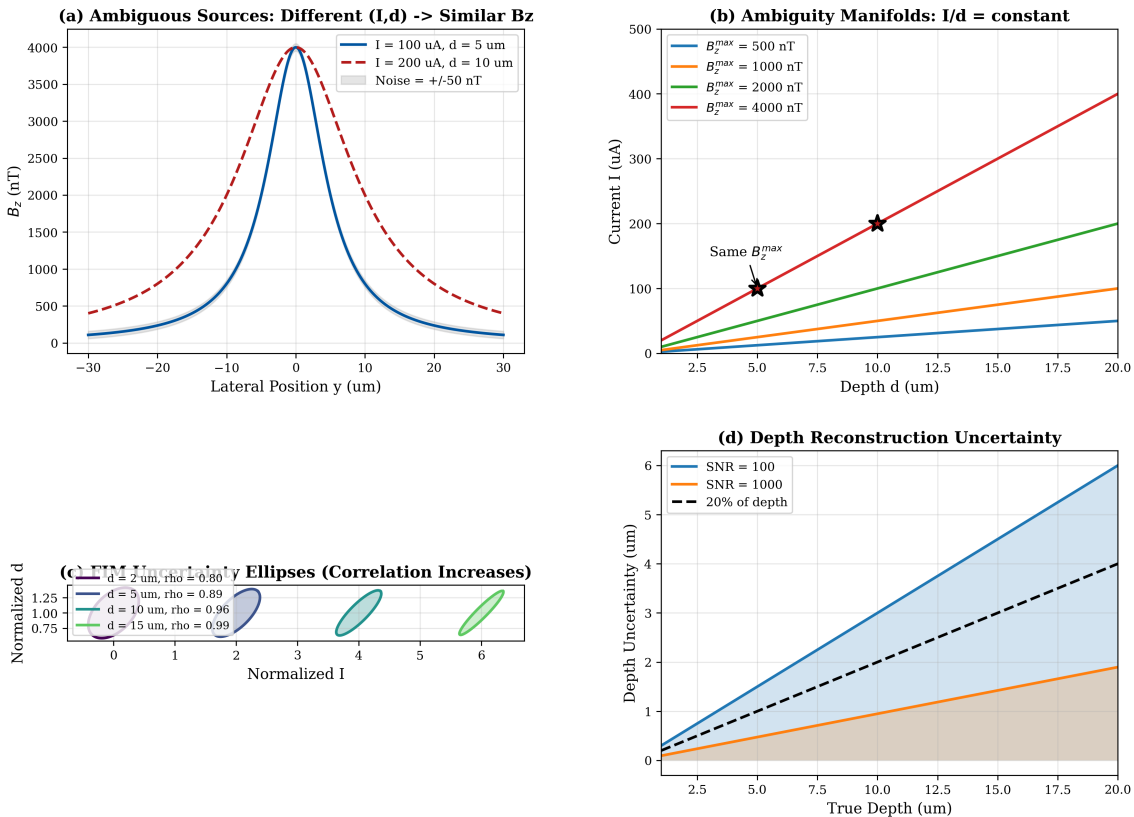


Figure 10.7: Depth-amplitude non-identifiability (Theorem 10.7.1). (a) Two sources with different  $(I, d)$  combinations producing statistically indistinguishable  $B_z$  profiles under band-limited noisy measurement. (b) Ambiguity manifold  $\mathcal{M}_\delta$  in  $(I, d)$  space; the manifold widens with increasing depth. (c) Fisher Information ellipse showing correlation  $|\rho_{Id}| \rightarrow 1$  as depth increases. (d) Reconstruction error vs. true depth showing systematic bias inherent to single-physics magnetic inversion.

### 10.7.3 Quantitative Impact on Reconstruction

The depth ambiguity limits single-physics reconstruction fidelity even with infinite SNR:

Table 10.6: Depth reconstruction accuracy for magnetic-only QFI

True Depth	Depth Uncertainty ( $1\sigma$ )	$\Gamma_{\text{inv}}$ Limit
1 $\mu\text{m}$	$\pm 0.3 \mu\text{m}$	0.85
5 $\mu\text{m}$	$\pm 2.1 \mu\text{m}$	0.65
10 $\mu\text{m}$	$\pm 5.8 \mu\text{m}$	0.45
20 $\mu\text{m}$	$\pm 15 \mu\text{m}$	0.25

For magnetic-only QFI, reliable depth determination is limited to:

$$d < 2z_0 \quad (10.46)$$

where  $z_0$  is the standoff distance. For sources deeper than  $2z_0$ , multi-physics measurements (Chapter 11) are required for unambiguous reconstruction.

### 10.7.4 Breaking the Ambiguity: Preview of Multi-Physics

The depth-amplitude ambiguity can be broken by incorporating additional physics channels with different depth dependencies:

- **Thermal:** Joule heating  $Q \propto I^2 R$ , with diffusion following  $T \propto 1/r$
- **Strain:** Thermoelastic expansion  $\epsilon \propto \alpha \Delta T$

The key insight: magnetic field scales as  $B \propto I/d$  while thermal signature scales as  $T \propto I^2$ . This nonlinear difference enables unique determination of both  $I$  and  $d$ . Chapter 11 develops this multi-physics approach in detail.

## 10.8 Design Rules for Magnetic QFI Systems

This section consolidates the key design rules derived throughout the chapter.

Use FFT-based forward models for regular grids with  $> 100 \times 100$  pixels. Use direct matrix methods only for irregular geometries or when boundary accuracy is critical.

Specify standoff distance based on required resolution  $\Delta x$  and target reconstruction fidelity  $\Gamma_{\text{inv}}^*$ :

$$z_0 \leq \frac{\Delta x}{\pi} \ln \left( \frac{\text{SNR}}{1/\Gamma_{\text{inv}}^* - 1} \right) \quad (10.47)$$

Sample the measurement grid at  $\Delta x \leq z_0/2$  to capture the effective resolution set by the standoff. Oversampling beyond this provides no information gain.

Allocate condition number budget as follows:

- $\kappa < 10^2$ : Direct inversion acceptable
- $10^2 < \kappa < 10^4$ : Tikhonov regularization required
- $10^4 < \kappa < 10^6$ : Advanced regularization (TV,  $\ell_1$ ) required
- $\kappa > 10^6$ : Multi-physics or strong priors mandatory

Implement multi-physics sensing (Chapter 11) when any of the following apply:

- Target depth  $d > 2z_0$
- Required  $\Gamma_{\text{inv}} > 0.85$  for  $\kappa > 10^3$
- Depth accuracy specification  $\sigma_d < d/3$

Table 10.7: Summary of magnetic forward model design rules

Parameter	Design Rule	Rationale
Standoff $z_0$	$z_0 < 1.5\Delta x$	Maintain $\Gamma_{inv} > 0.7$
Grid spacing $\Delta x$	$\Delta x \leq z_0/2$	Nyquist sampling
FOV size	$L > 10z_0$	Minimize boundary effects
SNR requirement	$SNR > \kappa/10$	Ensure $\Gamma_{inv} > 0.5$
Depth range	$d < 2z_0$ (magnetic-only)	Avoid ambiguity

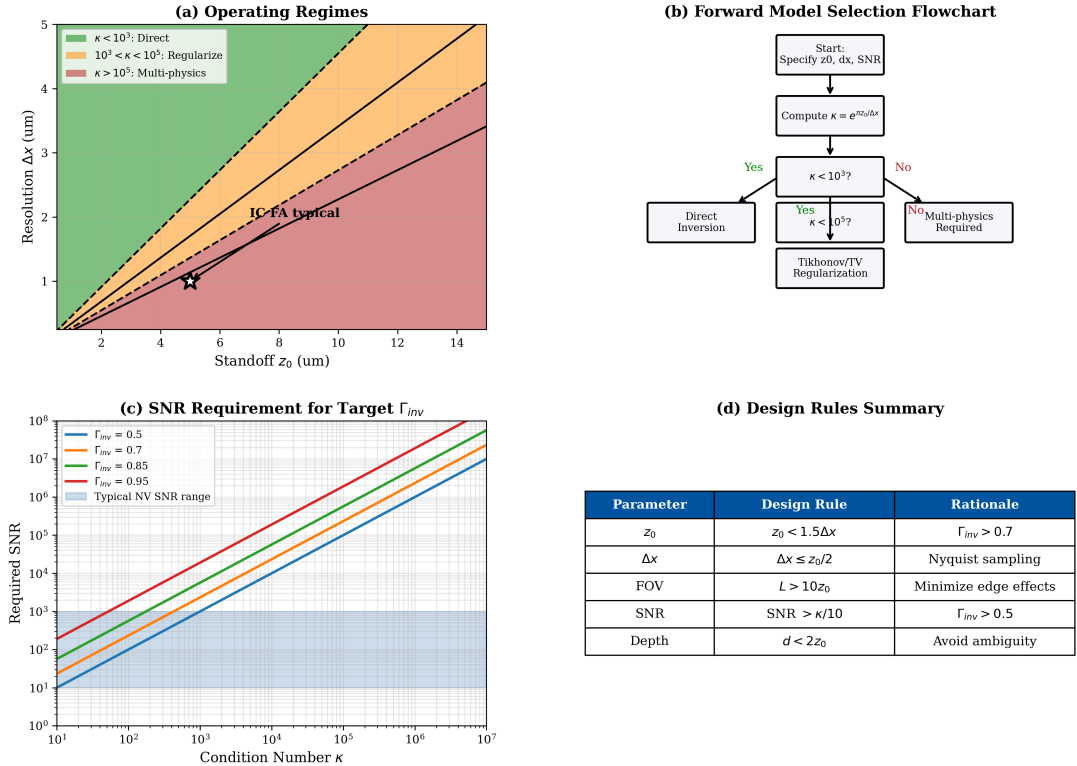


Figure 10.8: Design space for magnetic QFI systems. (a) Operating regimes in standoff–resolution space. Green region:  $\Gamma_{inv} > 0.85$  achievable. Yellow: requires regularization. Red: multi-physics mandatory. (b) Decision flowchart for forward model selection. (c) SNR requirements vs. target  $\Gamma_{inv}$  for different standoff ratios.

### 10.8.1 Model-Mismatch Fidelity $\Gamma_{mm}$ : Estimation Preview

Table 10.1 specifies a target  $\Gamma_{mm} > 0.95$  for the magnetic forward model. Achieving this requires controlling the dominant mismatch sources:

- Standoff calibration error:** Uncertainty  $\delta z_0$  in the sensor-to-source distance propagates as  $\delta\kappa/\kappa \approx (\pi/\Delta x)\delta z_0$ .
- Boundary truncation:** Finite FOV introduces convolution artifacts; the FOV sizing rule (Design Rule 10.8.2) mitigates this.
- NV layer depth spread:** The sensor is not a perfect plane; a depth distribution  $\sigma_{NV}$  blurs the effective Green’s function.
- Substrate and shielding effects:** Magnetic materials near the source distort the free-space Green’s function assumed here.

A practical  $\Gamma_{\text{mm}}$  estimation protocol—including calibration targets, residual whiteness tests, and model validation workflows—is developed in Chapter 14 (Section 14.6). For system design purposes, the forward model developed in this chapter achieves  $\Gamma_{\text{mm}} > 0.95$  when the standoff is calibrated to better than  $\delta z_0 < 0.1 \Delta x$  and the FOV exceeds  $10 z_0$ .

## 10.9 Worked Examples

### Example 10.9.1: Single Wire Current Mapping

**Problem:** A copper interconnect carries current  $I = 100 \mu\text{A}$  at depth  $d = 5 \mu\text{m}$  below a diamond NV sensor with standoff  $z_0 = 2 \mu\text{m}$ . Calculate the expected magnetic field profile and assess reconstruction feasibility.

**Given:**

- Current:  $I = 100 \mu\text{A} = 10^{-4} \text{ A}$
- Wire depth:  $d = 5 \mu\text{m}$
- Standoff:  $z_0 = 2 \mu\text{m}$
- Total distance:  $h = d + z_0 = 7 \mu\text{m}$
- Grid spacing:  $\Delta x = 0.5 \mu\text{m}$

**Solution:**

*Step 1: Calculate peak magnetic field*

$$B_z^{\max} = \frac{\mu_0 I}{2\pi h} \quad (10.48)$$

$$= \frac{4\pi \times 10^{-7} \times 10^{-4}}{2\pi \times 7 \times 10^{-6}} \quad (10.49)$$

$$= \frac{4 \times 10^{-11}}{14 \times 10^{-6}} \quad (10.50)$$

$$= 2.86 \times 10^{-6} \text{ T} = 2.86 \mu\text{T} = 2860 \text{ nT} \quad (10.51)$$

*Step 2: Calculate field profile width (HWHM)*

$$w_{\text{HWHM}} = h = 7 \mu\text{m} \quad (10.52)$$

*Step 3: Calculate condition number*

$$\kappa(\mathbf{G}) = e^{\pi z_0 / \Delta x} \quad (10.53)$$

$$= e^{\pi \times 2 / 0.5} \quad (10.54)$$

$$= e^{4\pi} \approx 2.87 \times 10^5 \quad (10.55)$$

*Step 4: Estimate reconstruction fidelity*

For typical NV sensitivity  $\sigma_B \approx 50 \text{ nT}$ , the SNR is:

$$\text{SNR} = \frac{B_z^{\max}}{\sigma_B} = \frac{2860}{50} \approx 57 \quad (10.56)$$

Expected reconstruction fidelity:

$$\Gamma_{\text{inv}} \approx \frac{1}{1 + \kappa/\text{SNR}} = \frac{1}{1 + 2.7 \times 10^5 / 57} \approx 0.0002 \quad (10.57)$$

**Conclusion:** Direct reconstruction will fail ( $\Gamma_{\text{inv}} \ll 0.1$ ). Options include: (1) reduce standoff, (2) increase SNR through averaging, or (3) apply multi-physics approach.

With standoff reduced to  $z_0 = 0.5 \mu\text{m}$ :

$$\kappa' = e^{\pi \times 0.5/0.5} = e^\pi \approx 23 \quad (10.58)$$

$$\Gamma'_{\text{inv}} = \frac{1}{1 + 23/57} \approx 0.71 \quad \checkmark \quad (10.59)$$

### Example 10.9.2: IC Power Grid Analysis

**Problem:** Analyze the forward model for a simplified IC power grid consisting of parallel metal lines with  $2 \mu\text{m}$  pitch at metal layer M1 (depth  $3 \mu\text{m}$  from surface).

**Given:**

- Line pitch:  $p = 2 \mu\text{m}$
- Line width:  $w = 1 \mu\text{m}$
- Metal fill: 50%
- Depth:  $d = 3 \mu\text{m}$
- Standoff:  $z_0 = 1 \mu\text{m}$
- Grid:  $128 \times 128$  pixels,  $\Delta x = 0.25 \mu\text{m}$

**Solution:**

*Step 1: Determine spatial frequency content*

The power grid has dominant spatial frequency:

$$k_{\text{grid}} = \frac{2\pi}{p} = \frac{2\pi}{2} = \pi \mu\text{m}^{-1} \quad (10.60)$$

*Step 2: Calculate transfer function at grid frequency*

$$|\tilde{G}(k_{\text{grid}}, z_0 + d)| = \frac{\mu_0}{2} e^{-k(z_0+d)} \quad (10.61)$$

$$= \frac{4\pi \times 10^{-7}}{2} e^{-\pi \times 4} \quad (10.62)$$

$$= 6.3 \times 10^{-7} \times e^{-12.6} \quad (10.63)$$

$$= 6.3 \times 10^{-7} \times 3.4 \times 10^{-6} \quad (10.64)$$

$$\approx 2.1 \times 10^{-12} \text{ T}\cdot\text{m}/\text{A} \quad (10.65)$$

*Step 3: Compare DC and grid-frequency components*

DC transfer (average current):

$$|\tilde{G}(0)| = \frac{\mu_0}{2} = 6.3 \times 10^{-7} \text{ T}\cdot\text{m}/\text{A} \quad (10.66)$$

Ratio (suppression of grid pattern):

$$\frac{|\tilde{G}(k_{\text{grid}})|}{|\tilde{G}(0)|} = e^{-12.6} \approx 3 \times 10^{-6} \quad (10.67)$$

**Conclusion:** The periodic grid pattern is suppressed by a factor of  $3 \times 10^{-6}$  relative to DC. Detecting individual lines requires either: closer standoff, higher SNR, or prior knowledge of the grid structure (CAD-informed reconstruction, Chapter 14).

### Example 10.9.3: Condition Number Computation

**Problem:** Compute the condition number of the Biot-Savart forward matrix for a  $64 \times 64$  grid with  $\Delta x = 1 \mu\text{m}$  and  $z_0 = 3 \mu\text{m}$ .

**Solution:**

*Step 1: Construct Fourier-domain kernel*

For each spatial frequency  $(k_x, k_y)$ :

$$\tilde{G}(k_x, k_y) = \frac{\mu_0}{2} e^{-\sqrt{k_x^2 + k_y^2} \cdot z_0} \quad (10.68)$$

*Step 2: Compute singular values*

The singular values are the absolute values of  $\tilde{G}$  evaluated on the discrete frequency grid:

$$k_x, k_y \in \left\{ -\frac{\pi}{\Delta x}, \dots, \frac{\pi}{\Delta x} \right\} \quad (10.69)$$

Maximum (at DC):  $\sigma_{\max} = \mu_0/2 = 6.28 \times 10^{-7}$

Minimum (at Nyquist corner,  $k = \sqrt{2}\pi/\Delta x$ ):

$$\sigma_{\min} = \frac{\mu_0}{2} e^{-\sqrt{2}\pi z_0/\Delta x} \quad (10.70)$$

$$= 6.28 \times 10^{-7} \times e^{-\sqrt{2}\pi \times 3} \quad (10.71)$$

$$= 6.28 \times 10^{-7} \times e^{-13.3} \quad (10.72)$$

$$= 6.28 \times 10^{-7} \times 1.7 \times 10^{-6} \quad (10.73)$$

$$\approx 1.0 \times 10^{-12} \quad (10.74)$$

*Step 3: Compute condition number*

$$\kappa(\mathbf{G}) = \frac{\sigma_{\max}}{\sigma_{\min}} = \frac{6.28 \times 10^{-7}}{1.0 \times 10^{-12}} \approx 6 \times 10^5 \quad (10.75)$$

*Step 4: Verify with analytical formula (2D corner bound, Corollary 10.6.1)*

$$\kappa_{2D} = e^{\sqrt{2}\pi z_0/\Delta x} = e^{13.3} \approx 6 \times 10^5 \checkmark \quad (10.76)$$

Note: The 1D axial bound (Theorem 10.6.1) gives  $\kappa_{1D} = e^{\pi \times 3} = e^{9.4} \approx 1.2 \times 10^4$ , a factor of  $\sim 50$  lower. This example confirms the conservative 2D bound.

**Result:** Condition number  $\kappa(\mathbf{G}) \approx 6 \times 10^5$ , indicating that regularization is mandatory for stable reconstruction.

## 10.10 Chapter Summary

This chapter established the mathematical foundation for magnetic field forward models in Quantum Field Imaging:

1. **Biot-Savart Fundamentals:** The forward model  $\mathcal{G}_B$  is derived from Maxwell's equations, expressing the magnetic field as a convolution of current density with the Green's function kernel.
2. **Exponential Decay:** In Fourier space, the transfer function  $|\tilde{G}(k)| \propto e^{-kz}$  causes exponential suppression of high spatial frequencies, fundamentally limiting resolution.
3. **Condition Number Scaling:** The forward matrix condition number scales as  $\kappa_{1D} = e^{\pi z_0/\Delta x}$  (1D axial bound) or  $\kappa_{2D} = e^{\sqrt{2}\pi z_0/\Delta x}$  (2D worst-case corner), growing exponentially with the standoff-to-resolution ratio.

4. **Reconstruction Fidelity Limit:** Single-physics magnetic QFI is limited to  $\Gamma_{\text{inv}} < 0.7$  for sources deeper than twice the standoff distance.
5. **Depth-Amplitude Ambiguity:** Magnetic measurements alone cannot uniquely determine both source depth and current magnitude, motivating multi-physics approaches.
6. **Design Rules:** Quantitative guidelines link standoff distance, grid spacing, SNR, and target  $\Gamma_{\text{inv}}$  to enable system specification.

**Connection to Following Chapters:**

- Chapter 11 develops multi-physics forward models that break the depth-amplitude ambiguity
- Chapter 14 presents reconstruction algorithms  $\mathcal{R}$  that address the ill-conditioning analyzed here
- Chapter 15 applies these forward models to IC current density reconstruction

## Problems and Solution Hints

### Problem 10.1: Biot-Savart for Circular Loop

Derive the magnetic field  $B_z(0, 0, z)$  on the axis of a circular current loop of radius  $a$  carrying current  $I$ . Show that the result reduces to the dipole formula for  $z \gg a$ .

**Hint:** Use the Biot-Savart law in cylindrical coordinates. The integral simplifies due to symmetry. For the dipole limit, expand to leading order in  $a/z$ .

### Problem 10.2: Condition Number Derivation

Prove that for a 1D Biot-Savart problem (wire parallel to sensor array), the condition number is exactly  $\kappa = e^{\pi z_0 / \Delta x}$ .

**Hint:** The 1D problem is diagonal in Fourier space. Compute the eigenvalues directly from the transfer function.

### Problem 10.3: Depth Ambiguity Quantification

For a point dipole source, compute the Fisher Information Matrix for parameters  $(m, z)$  where  $m$  is the dipole moment magnitude and  $z$  is the depth. Show that the correlation coefficient approaches 1 as depth increases.

**Hint:** The field is  $B_z \propto mz/(x^2 + z^2)^{5/2}$ . Compute  $\partial B_z / \partial m$  and  $\partial B_z / \partial z$ , then form the FIM.

### Problem 10.4: FFT Implementation

Implement an FFT-based forward model for the 2D Biot-Savart problem. Verify against direct summation for a test current distribution. Compare computation times for grid sizes from  $32 \times 32$  to  $1024 \times 1024$ .

**Hint:** Use zero-padding to handle circular convolution artifacts. The FFT kernel should be pre-computed for efficiency.

### Problem 10.5: Multi-Layer Forward Model

Extend the single-layer forward model to handle currents distributed across  $N$  metal layers at different depths  $\{d_1, d_2, \dots, d_N\}$ . Analyze how the condition number depends on the number and spacing of layers.

**Hint:** The combined forward matrix is  $\mathbf{G} = [\mathbf{G}_1 | \mathbf{G}_2 | \cdots | \mathbf{G}_N]$  where each  $\mathbf{G}_i$  corresponds to depth  $d_i$ . The condition number depends on whether the column spaces overlap.

### Problem 10.6: Optimal Standoff

For a QFI system targeting  $\Gamma_{\text{inv}} > 0.8$  with SNR = 200 and resolution  $\Delta x = 0.5 \mu\text{m}$ , determine the maximum allowable standoff distance.

**Hint:** Invert the  $\Gamma_{\text{inv}}$  formula to solve for  $z_0$  in terms of  $\kappa$ , then use the exponential scaling relation.

## References

- [1] J. D. Jackson, *Classical Electrodynamics*, 3rd ed. (Wiley, 1999), Ch. 5.
- [2] D. J. Griffiths, *Introduction to Electrodynamics*, 4th ed. (Cambridge University Press, 2017), Ch. 5.
- [3] M. S. Hämäläinen, R. Hari, R. J. Ilmoniemi, J. Knuutila, and O. V. Lounasmaa, “Magnetoencephalography— theory, instrumentation, and applications to noninvasive studies of the working human brain,” *Rev. Mod. Phys.* **65**, 413–497 (1993).
- [4] J.-P. Tetienne *et al.*, “Quantum imaging of current flow in graphene,” *Sci. Adv.* **3**, e1602429 (2017).
- [5] D. A. Broadway *et al.*, “Improved current density and magnetization reconstruction through vector magnetic field measurements,” *Phys. Rev. Applied* **14**, 024076 (2020).
- [6] I. Fescenko *et al.*, “Diamond magnetometer enhanced by ferrite flux concentrators,” *Phys. Rev. Research* **2**, 023394 (2020).
- [7] P. Kehayias *et al.*, “Imaging crystal stress in diamond using ensembles of nitrogen-vacancy centers,” *Phys. Rev. B* **100**, 174103 (2019).
- [8] A. Tarantola, *Inverse Problem Theory and Methods for Model Parameter Estimation* (SIAM, 2005).
- [9] P. C. Hansen, *Discrete Inverse Problems: Insight and Algorithms* (SIAM, 2010).
- [10] C. R. Vogel, *Computational Methods for Inverse Problems* (SIAM, 2002).